Overview of steady-state tokamak operation and current drive experiments in TRIAM-1M

H. ZUSHI, K. NAKAMURA, K. HANADA, K.N. SATO, M. SAKAMOTO, H. IDEI, M. HASEGAWA, A. IYOMASA, S. KAWASAKI, H. NAKASHIMA, A. HIGASHIJIMA, T. KURAMOTO[1)], A. TANAKA[1)],Y. MATSUO[1)], K. ESAKI[1)], H. AKANISHI[1)], H. AYATSUKA[1)], S. IMADA[1)], T. SUGATA[1)], H. HOSHIKA[1)], K. SASAKI[1)], N. MAEZONO[1)], M. KITAGUCHI[1)], N. IMAMURA[1)], T. HAYASAKI[1)], K. ICHIZONO[1)], S. KUGIMIYA[1)], N. YOSHIDA, K. TOKUNAGA, T. FUJIWARA, M. MIYAMOTO[1)], M. TOKITANI[1)], K. UEHARA[2)], Y. SADAMOTO[3)], Y. NAKASHIMA[4)], Y. KUBOTA[4)], Y. HIGASIZONO[4)], Y. TAKASE[5)], A. EJIRI[5)], S. SHIRAIWA[5)], S. KADO[5)], T. SIKAMA[5)], S. TSUJI-IIO[6)],T. TAKEDA[7)], Y. HIROOKA[8)], K. IDA[8)], Y. NAKAMURA[8)], T. FUJIMOTO[9)], A. IWAMAE[9)], T. MAEKAWA[9)], O. MITARAI[10)]

Advanced Fusion Research Center, Research Institute for Applied Mechanics, Kyushu University, Kasuga 816-8580, Fukuoka, Japan, Interdisciplinary Graduate School of Engineering Sciences, Kyushu University[1)], Japan Atomic Energy Research Institute[2)], Joetsu University of Education[3)], University of Tsukuba[4)], The University of Tokyo[5)], Tokyo Institute of Technology[6)], The University of Electro-Communications[7)], National Institute for Fusion Science[8)], Kyoto University[9)], Kyushu Tokai University[10)]
E-mail: zushi@triam.kyushu-u.ac.jp

Abstract Experiments aiming at ‘day long operation at high performance’ have been carried out. The record value of the discharge duration was updated to 5 h and 16 min. Steady-state tokamak operation (SSTO) is studied under the localized PWI conditions. The distributions of the heat load, the particle recycling flux and impurity source are investigated to understand the co-deposition and wall pumping. Formation and sustainment of an internal transport barrier ITB in enhanced current drive mode (ECD) has been investigated by controlling the lower hybrid driven current profile by changing the phase spectrum. An ITER relevant remote steering antenna for electron cyclotron wave ECW injection was installed and a relativistic Doppler resonance of the oblique propagating extraordinary wave with energetic electrons driven by lower hybrid waves was studied.

1. Introduction

With the goal of addressing the critical issues of steady-state tokamak operation (SSTO) [1,2,3] of future fusion devices, experiments aiming at ‘day long operation at high performance’ have been carried out in a limiter configuration of TRIAM-1M plasma (R_0 =0.84 m, a~0.12 m and B = 6-7 T). Concerning with SSTO, three areas (temporary changes in wall pumping, formation and steady state sustainment of internal transport barrier ITB, and current drive by electron cyclotron ECW) are investigated. The record value of the discharge duration was updated to 5 h and 16 min (Fig. 1a) by localizing the particle recycling profile at a limiter with high heat removal capability and by reducing the surface temperatures of plasma facing components PFCs [4]. Total 0.11GJ energy is deposited on the PFCs. In order to understand wall pumping [5], recycling and heat load distribution, impurity source and deposition rate, surface temperature, the thickness of the metal film and hydrogen retention were investigated. In the study of the enhanced current drive ECD mode [1,6,7], an ITB for the ion temperature profile Ti(r) was found near the threshold power for ECD transition. Physics of the transition associated with ITB formation [8-10] and current profile effects on the sustainment of ECD/ITB modes were investigated. Current profile control by ECW is indispensable to SSTO from view points of stability and high performance [11]. A remote steering antenna was developed for 170GHz and oblique extraordinary OX-mode current drive ECCD [12,13] was carried out under the ITER relevant condition [14]. An ECCD scenario of up-shift relativistic Doppler resonance was tested in full current drive plasmas by LHW, in which energetic electrons can be resonant with OX-mode.

In this paper, recent SSTO experimental results in TRAIM-1M since last IAEA conference [1] are presented. It is organized as follows. In section 2, a world record discharge is investigated from the several viewpoints, such as particle recycling, heat load distribution, metal impurity (Mo) deposition rate, and hydrogen retention. PWI induced ultra low frequency ULF (~10^{-3} Hz) and termination events are also discussed. In section 3, probability

aspects of the transition of ECD are investigated in the power hysteresis window. Self-organized slow sawtooth oscillations SSSO are discussed with respect to the high performance sustainment. In section 4, the results of OX-mode off-axis current drive will be presented. Finally, we will summarize the results.

2. Steady state tokamak operation

2-1 Plasma facing components

In order to investigate the PWI effects on SSTO from a view point of heat load, particle recycling and impurity influx distributions, a water cooled rail limiter (movable limiter; ML) was inserted vertically into the plasma and thus the main contribution of the PWI could be localized on ML. Other plasma facing components PFCs consist of three D-shaped limiters PLs, divertor plates DPs, vacuum vessel, the cover of bellows, and LH antenna. The ML and the one of PLs are located at the external pumping port. The ML, PLs and DPs are made from molybdenum, and others are stainless-steel. The closest distances from the last closed flux surface LCFS determined by the ML are ~5mm for the inner mid-plane part of PL, ~24 mm for outer one, ~46mm for DPs, 22mm for inner wall, ~41 mm for outer one, and ~46 mm for LH antenna, respectively. Since the ML with high cooling capability is used, the surface temperatures of PFCs could be successfully reduced by ~100 K compared with those in discharges with PLs, in which configuration the contact part of PLs to the plasma on the mid-plane is not directly cooled [15]. The IR measured surface temperature of ML is less than 600K. T_{wall} and $T_{limiter}$ of PLs could be reduced to 330K and 450K, respectively. The temperature rise of the in vessel PFCs was kept to be lower by 70 – 100 K than the previous experiments with using PLs.

2-2 Diagnostics for recycling, heat load, impurity influx, dust, and hydrogen retention

Since the complex processes of particle recycling are thought to functions of the particle flux and heat load, surface temperature and thermal stability of the deposited layer, energy of the recycling particles and impurity source, surface modification (re-deposition) and hydrogen retention in the deposition layer, the following diagnostics are used.

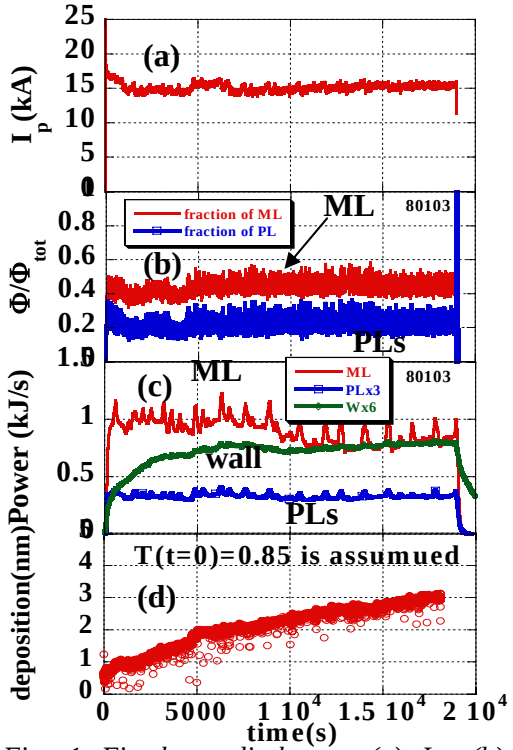

Fig. 1 Five-hour discharge; (a) Ip, (b) fractions of recycling particles,(c) heat load on PFCs, and (d) Mo deposition thickness.

An H_α measurement system consists of fiber optics, narrow H_α filters and photomultipliers is used to measure toroidal (six positions; Z m along the torus) and poloidal (seven vertical chords along the major radius; ΔR=-80~+75 mm) distributions. From this measurement the toroidal distribution and fraction of the recycling flux from PFCs was deduced (Fig. 1b). A fan array fiber with horizontal twenty five chords attached to a spectrometer is also used to evaluate the hydrogen influx profile (656 nm) and energy components of hydrogen atoms [16]. At the same port a spectroscopy covered with a wide wavelength range (200-800 nm) is installed to monitor the history of discharges or the time evolution of the spectra in the visible range during the shot. The feedback control of the hydrogen influx is performed with a spectroscopy fixing at H_α line. As an actuator of the particle influx control, the H_α monitor signal is used at the position of 0.64m from ML and 2.2m from the gas puffing port.

A calorimeter system with 32 thermistors for cooling water temperature of PFCs is used to evaluate the distribution of the heat load

deposited on the PFCs(Fig. 1c) [17,18]. The cooling units for the wall are divided into six loops and DPs eight loops. The each PL is measured independently. The temperature difference of the inlet and outlet cooling water is 0.2 K to 1.5 K for the flow rate from 4 l/min to 90 l/min.

The main metal impurity ions are Mo. Visible (Mo I 386 nm) and VUV (Mo XIII 34.1nm) spectrometers are used to determine the Mo influx and to study accumulation. The source profile of the Mo atoms is measured by a spectrometer viewing the wall and DPs or the ML. In situ measurement of metal (Mo) deposition thickness on the window was carried out. From the measurement of the transmittance of the plasma light through this viewing window made of sapphire and the assumption that the Mo atoms were deposited on it, the deposition rate Γ_{Mo}^{dep} of 1.1×10^{16} Mo/m^2/s was determined [4] (Fig. 1d).

The bulk surface and dust temperatures of ML are measured by an IR camera at 3-3.5 μm and a near IR spectrometer from 0.9 μm to 1.65 μm. By assuming that the observed spectrum $I^{obs}(T_{obs})$ is the sum of $I_{BB}(T_b)+\varepsilon I_{BB}(T_d)$, T_b, T_d and ε are deduced[19], where I_{BB} the black body radiance, T_b and T_d bulk and dust temperatures, respectively and ε the fraction of the dust covering area to the total viewing area. According to this method and the observed near IR spectrum it is observed that T_d can reach the melting temperature of Mo and ε up to a few %. During the discharge, the frequency of Mo spikes measured by influx monitor and soft X-rays increase toward the end. This is consistent with the temporal increase in ε.

The crystallization, thickness and hydrogen retention of deposited Mo on SUS/W/Si specimens attached on the surface probe system were studied [20]. After exposing specimen to single or multi discharges, crystallization is studied by transmission electron microscopy TEM, the thickness is evaluated by Rutherford backscattering spectroscopy RBS with 2MeV He^+ beam and the hydrogen retention is by elastic recoiled detection ERD with 2.8MeV He^+ beam. In case of ERD, the beam fluence was simultaneously monitored by RBS. The probe head is located in the SOL at 5 mm behind the surface of the PL. The specimens are located at the plasma facing side P-side. The radial profile of deposited Mo thickness and retained H are obtained from 5 mm to 20 mm in the electron drift side E–side in the SOL. It has been also found that grain size and crystallization of Mo depend on the discharge duration, oxygen content, and the location of the specimen [21].

2-3 Toroidal distribution of the recycling flux and contribution of the ML

During 5 hour discharge, H_α intensities for initial 500~1000 s can be fitted by $\sum A_i \exp(-t/\tau_i)$, where A_i and τ_i are amplitude and time constants of 5s, 50s and 2000 s, for example. Then they are kept constant by feed back controlled gas puffing. The normalized poloidal profiles at the different toroidal locations are found to be almost the same, although the intensity at the ML is extremely high indicating the toroidally localized particle recycling. The toroidal distribution at 18000s is shown in Fig.2. In order to evaluate the fraction of particle source rate we used the following simple relation [22]

$$\dot{N} = 2\pi a(\Phi_w 2\pi R + \Phi_{ML}\lambda_{ML}\sqrt{\pi} + 2\Phi_{PL}\lambda_{PL}\sqrt{\pi})$$

where $\Phi_{w,ML,PL}$, $\lambda_{ML,PL}$ are flux determined from H_α intensity and characteristic toroidal length, respectively. The spectrum analysis based on the Zeeman effects and a two-temperature model [8] for the H_α line shows the fraction of energetic hydrogen atoms with ~ 6 eV is twice that of the low energy atoms of ~0.4eV. The λ is consistent with the Monte Carlo calculations done in Gamma-10 with similar parameters [23]. In Fig. 1b the fraction of each component is shown during the discharge and the ML contributes ~ 40% of the total particle recycling source rate. The total sum of three PLs is 20 % and the rest is the sum of wall and DPs. For the discharge cleaning by ECR (2.45 GHz) at the low filed there was no significant toroidal structure, which indicates that the λ is the order of the torus circumference because of the low density.

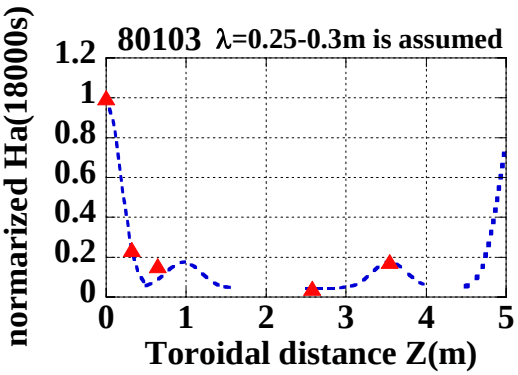

Fig.2 The toroidal distribution of H_α (triangles). Dotted curves are fitted curves.

2-4 Toroidal distribution of heat load

As shown in Fig. 1(c), after 5000 s, the steady state is established for the temperature profiles. This very long required time is due to particular two of the six wall cooling loops, on which the fractional turns for poloidal coils are installed. A fraction of 34 % of the total heat load is deposited on the ML, which is the same order of the particle recycling fraction. The rest is distributed on PLs (10%), and wall (34%) and divertor plates (22%)[18]. For t=17500 s - 18500 s the averaged heat flux <q> distribution is shown in Fig.3. Here the averaged heat flux on each PFC is defined by the measured heat load divided by the interaction surface area. For walls the minimum points correspond to those with very long equilibrium time constants. Although the covered area is smaller than others, <q> is also lower than those. This n=2 like toroidal structure for the wall is under consideration. For ML, although <q> is ~ 0.3 MW/m^2, q_{peak} reaches 4 MW/m^2 on the bright area.

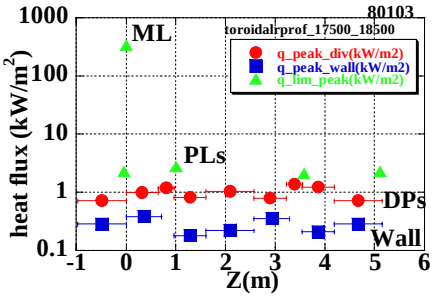

Fig.3 The toroidal distribution of the average heat flux on each PFCs.

2-5 Metal source profile and in situ measurement of Mo deposition flux

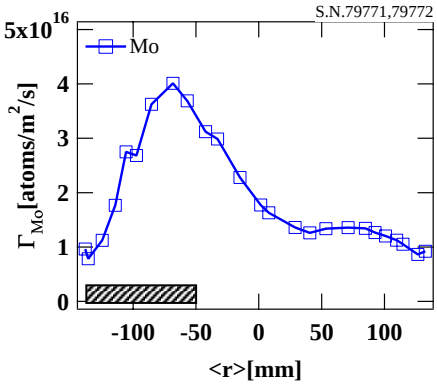

Fig.4 MoI profile vs. the tangent radius $<r>_{tan}$. The shaded area is DP.

The influx Γ_{Mo} is determined ~ 3-4 x10^{16} Mo atoms/m^2 s. Although H_α and OII profiles are up-down symmetry, $\Gamma_{Mo}(<r>_{tan})$ shows a significant asymmetry, as shown in Fig. 4. It is considered that MoI originates from the DP located at the lower part of the chamber located from $<r>_{tan}$= -50 to -140 mm. From sputtering yields [24], and ratios of Γ_{Mo}/Γ_O and Γ_{Mo}/Γ_H, we consider that oxygen ions mainly contribute Mo sputtered yield. These atoms are ionized with a very short mean free path in the plasma edge, but the some atoms can penetrate through the scrape off layer SOL and finally stick the viewing window located at the 75 mm from the last closed flux surface. The attenuation factor along the path in the SOL is evaluated 0.3.

2-6 Relation between the Mo thickness and H retention

The data for SUS/W specimen were taken for a single 72 min discharge with the ML[20]. Figure 5 shows the amount of retained hydrogen in W specimens as a function of the thickness of the deposited Mo. A clear correlation was observed between the retained hydrogen and the Mo thickness, indicating the co-deposition of hydrogen with Mo. The TEM images indicate that there are differences from grain size and crystallization of the deposited Mo, especially for P and E side. The Γ_{Mo}^{dep} are3.9×10^{17} Mo/m^{2}s for E-side specimen located at 7 mm behind the PL and 0.64×10^{17} Mo/m^{2}s for P-side, respectively. The difference between them is considered to be due to variations in the sticking rate and sputtering rate depending on elementary processes in plasma surface interaction. If we

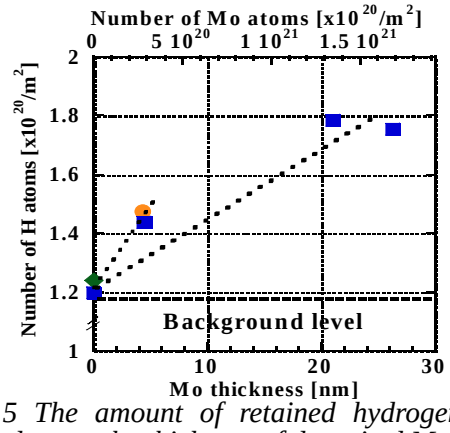

Fig. 5 The amount of retained hydrogen dependent on the thickness of deposited Mo

can extrapolate a twofold radial profile of Γ_{Mo}^{dep} in the SOL to the faraway window, the spectroscopically determined Γ_{Mo}^{dep} is consistent. The retained hydrogen fluxes, that is, wall pumping fluxes Γ_{wall} are estimated to be ~ 1.3×10^{16} H/m^{2}s and 0.64×10^{16} H/m^{2}s, respectively. The ratio of H/Mo of 0.04 to 0.1 was also evaluated. The global particle balance analysis with a simple assumption of the wall surface area of 5 m^2 give the Γ_{wall} ranging from ~ 1.5×10^{16} H/m^{2}s [25] to 8.55×10^{16} atoms/m^{2}s [26]. These values are less than 1 % of the hydrogen influx (~ 3×10^{18} H/m^{2}s) determined by spectroscopic measurement.

2-7 Wall inventory in SSTO

According to the facts of no spectroscopic observation of Fe, Cr and Ni influxes and a very few (at.%) depositions of them on the specimens measured by RBS [20,27] we consider that the inner surface of the wall is covered by a Mo thin layer with thickness of at least a few nm, by which no sputtering of SUS is expected for 1 keV H atom injection. Using H/Mo of 0.07 and the surface density of 3×10^{20} Mo atoms/m^2 corresponding to Mo thickness of ~ 4 nm the wall inventory can be calculated ~ 4.6×10^{20} H atoms for 5 hour discharge. This is ~ 1/20 smaller than that shown in Fig. 6. In order to investigate the toroidal structure of the wall inventory the temperature dependent H release process, microstructure dependent H/Mo, and detailed Mo source profile must be monitored in future devices.

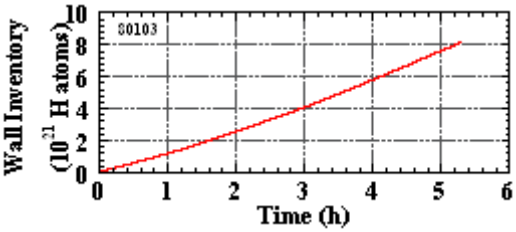

Fig. 6 Wall inventory during 5 hour discharge.

2-8 Ultra low frequency ULF events

As shown in Fig. 7, PWI driven relaxation oscillations (ULF events) are observed on heat load, recycling flux and impurity behavior [28]. These oscillations are semi-regular and should be distinguished from the random off-normal events. We are concerned with this oscillation because the 5 hour discharge has terminated during the last event (see 2-9). ULF events are characterized by slow variations and quick decay. “Slow phase” lasts for 150 s ~ 200 s and “quick decay phase” ~50 s-100 s. ULF events are repeated at the frequency of

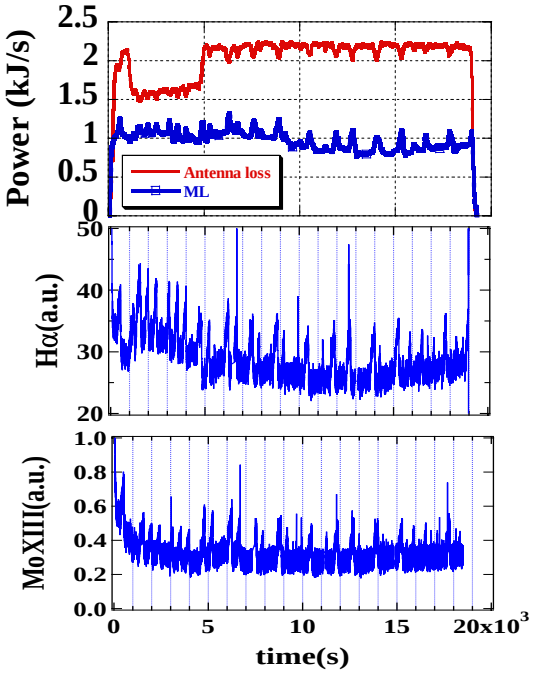

Fig. 7 Heat load, recycling flux and Mo XIII in five-hour discharge. Perturbations with 1-2x10^{-3}Hz are seen on these signals.

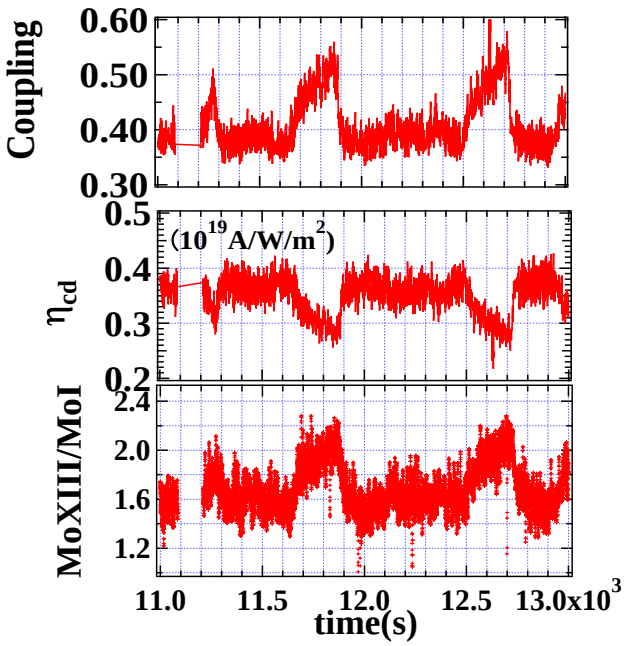

Fig.8 The rf coupling, current drive efficiency, impurity accumulation factor for ULF events.

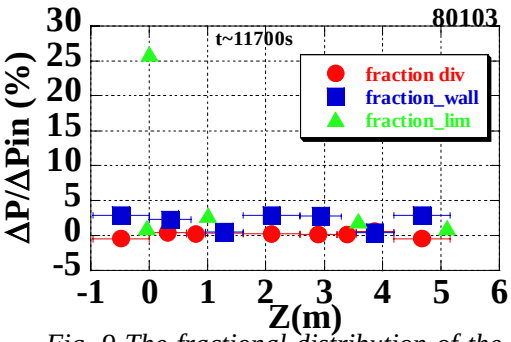

Fig. 9 The fractional distribution of the variation in heat load deposited on PFCs durina the ULF event.

1-2x10^{-3} Hz. The coupling is defined as the ratio of the net launched power including the antenna loss of ~0.14 to the constant incident LHW power. It maintains ~ 40 % whole duration, but increases to 50 % during the ULF event. As a consequence Ip increases by ~ 3%. Thus, the current drive efficiency ($\eta_{CD}= I_p R n_e / P$) shows a reduction from 0.37 to 0.28 x 10^{19} A/Wm^2. This unfavorable aspect is considered to be due to the impurity accumulation, which is suggested from the accumulation factor defined as a ratio of MoXIII to Mo I, as shown in Fig. 8. The core impurity transport change during the ULF event is under study.

The total power change ΔP_{in} in event is evaluated of < 1 kW. The summing up the total power change in all PFCs gives 0.44 kW, half the ΔP_{in}, because the ULF duration of ~ 200 s is not enough to estimate the deposited energy. The fraction of the heat load deposited on PFCs during the ULF events is shown in Fig.9. Although the uncounted power exists, the largest fraction was still localized on the ML. When the ULF event occurs the heat load on the ML starts to increase linearly at the rate of ~ 1.5±0.2 W/s, and then decays at the same or lower rate. This aspect is different from those of the impurity or recycling flux. The ULF event causes outward shift of $H_\alpha(\Delta R)$, which is favorable for the coupling. The variation of H_α is 8% at $\Delta R=0$ and 35 % at $\Delta R=70$ mm. After a lapse of ~ 200 s from the trigger time of ULF event $H_\alpha(\Delta R)$ shifts back to the previous one within ~ 50 sec, because of temporally shut-off of the piezo-valve by feedback loop, but after that several H_α bursts corresponding to those of gas puffing are seen. The $H_\alpha(\Delta R)$ shifts inward at the burst, in the opposite direction compared to the slow variation of ULF. The $H_\alpha(Z)$ shows a highly localized profile near the ML, but the variation $\Delta H_\alpha(Z)$ seems to be uniform around the torus.

2-9 Termination of the steady state discharge

The 5 hour discharge was stopped at $t=t_{end}$ (=18973.8 s) without a sign of termination. The last ULF event starts ~ -150 s before t_{end} and seems to continue similar to the previous ones. An intense perturbation was thought to occur at t_1=-2.1 s, as shown in Fig. 10(a). The current dropped by -25 % within 0.2 s, but it could be recovered to the previous level of 16 kA within following 0.8 s. However, the second intense perturbation at t_2=-1.1 s leaded the current quench. Although the quench rate dIp/dt=-6 kA/s was smaller that -20kA/s of the first one, current decay could not be recovered. Figure 10 (b) and (c) show the $\Delta H_\alpha(Z)$ and $\Delta H_\alpha(\Delta R)$ profiles at the first perturbation. The toroidal structure is quite complicated. At the ML the $\Delta H_\alpha(Z=0)$ is negative at t_1 and then becomes positive. $\Delta H_\alpha(Z)$ at the PL is always positive. The negative variation indicates the reduction in PWI. $\Delta H_\alpha{}^9(\Delta R)$ at the PL shows a strong in-out asymmetry but $\Delta H_\alpha{}^1(\Delta R)$ at ML does not show such one, indicating that the enhanced PWI in the outboard side occurs locally at the particular PFCs. At the second perturbation above mentioned aspects in both profiles of $\Delta H_\alpha{}^9(\Delta R)$ and $\Delta H_\alpha(Z)$ are the same as the first one, but the amplitudes is larger. Finally the current is quenched.

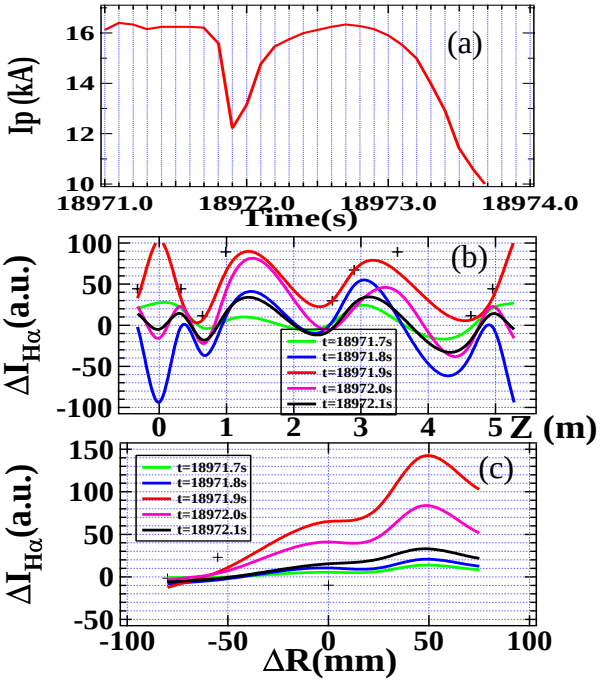

Fig10 Two intense events ~ 2 s before the termination. (a)Ip(t), $\Delta H_\alpha(Z)$ (b) and $\Delta H_\alpha{}^9(\Delta R)$ (c) at the termination phase.

3 Enhanced Current Drive mode

3-1 ITB in ECD mode

The SSTO of the high performance is studied from a view point of the ITB formation and sustainment [10]. It was found in the full current drive plasma that the ITB for ion energy transport is formed at r/a~0.3 and the ion temperature gradient ∇T_i of 4~5 keV/m was achieved in the ECD mode. The ITB structure was studied as a function of the hard X-rays profile H(R), which indicates a profile of the current carrying energetic electrons of from 40 keV to ~250 keV and is sensitive to the ECD transition. The current profile effects on back-transition have been studied by slow power ramp-down technique (-14 kW/s ~ -23 kW/s) for several seconds. It is found that the ∇T_i inside r/a <0.3 well relates to the H(R) gradient ∇H for r/a < 0.2 around the back transition. As the LHCD power deceased, ∇H decayed gradually, and then the back-transition was triggered. The ∇T_i changed rapidly and H(R) became broad. The complete transition to non-ECD mode took 0.2-0.5 s, which are several tens of the energy confinement time. This very long transient phase suggests that there exists an intermediate state during the transition from ECD to non-ECD states.

3-2 Ti- ITB and current profile in the intermediate state

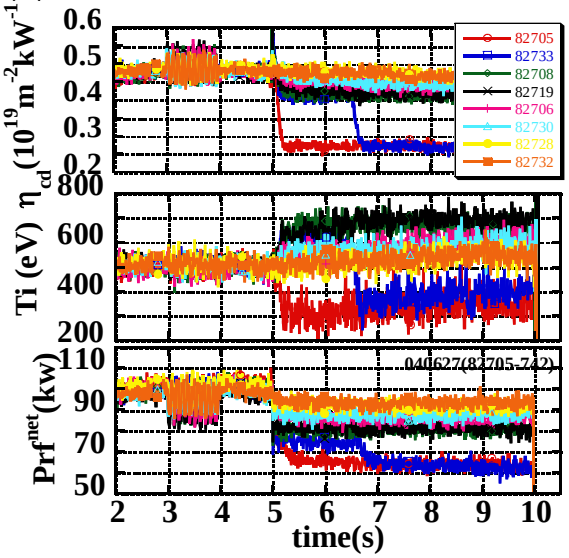

Fig. 11 Power step down at 5 s (ECD t<5 s);(a) η_{CD},(b) T_i, and (c) P_{LH}

In order to confirm this, the following experiments are conducted. The ECD state is sustained stably at P_{LH}~100kW for a few second and then the power is step down to 65 kW by ~5% per each shot. According to this step power down, Ip decreased from 43 kA(ECD) to 27 kA and n_e decreased from 1.3×10^{19} m^{-3} (ECD) to 0.75×10^{19} m^{-3}, however, it is found that Ti increased 0.7 keV for a particular power range, as shown in Fig.11. Although η_{CD} is classified into two groups ($0.5\text{-}0.4\times10^{19}$A/$m^2$/W or 0.28×10^{19}A/m^2/W), the highest group of τ_{ion} of 5 ms appeared in addition to two groups (3-4.2 ms or 1.5-2 ms). Here τ_{ion} is defined $1.5n_eT_i(0)Vp/P_{LH}$ as a measure of the ion energy replacement time. This intermediate state is characterized by high ion temperature with an ITB, as shown in Fig.12. The foot point is around 3.7 cm and ∇T_i inside of this radius is ~10 keV/m, which is twice as much as ∇T_i in ECD.

In order to estimate the change in the current profile associated with ITB, a peaking factor f_{HX} of the hard X-ray profile and internal inductance *li* from the magnetic measurement are investigated. We assume the fixed pressure profile of $(1-(r/a)^2)^2$ and the fixed ratio of Te/Ti of 1.6 to evaluate βp and neglect the contribution of tail electrons to βp. In ECD *li* is ~1.2, and then it changes to ~0.8 (ITB) or 1.9 (non-ECD). That is, it can be considered that the current profile $j_{LH}(r)$ is changed from the peaked one to broad one when the ITB is formed. In non-ECD mode it is peaked. The tendency of f_{HX} is reversed with respect to ITB formation. It is highest ~2.1 for ITB and ~1.9 for ECD, ~1.7 for non ECD, respectively. The power modulation technique is used to evaluate the deposition power profile [29]. The

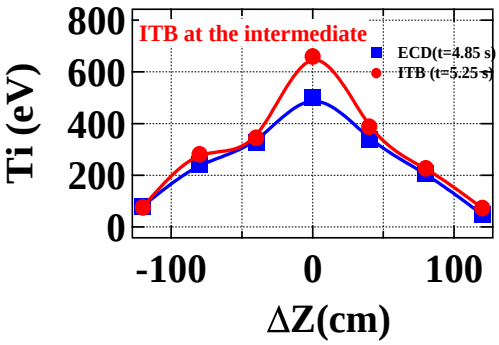

Fig. 12 Ti profiles for ITB and ECD. The foot point is z=3.7 cm

result shows that the power deposition near the foot point is essential to form ITB.

3-3 Transition probability

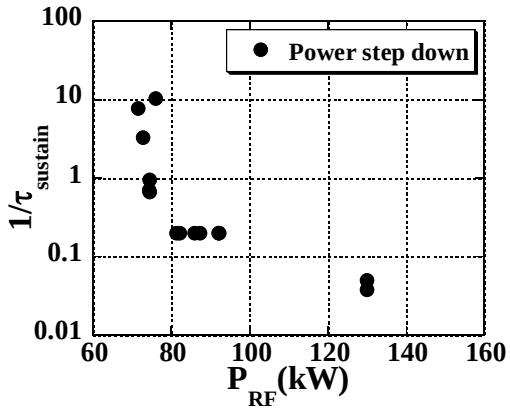

Fig.13 The transition probability ($1/\tau_{life}$) vs. power.

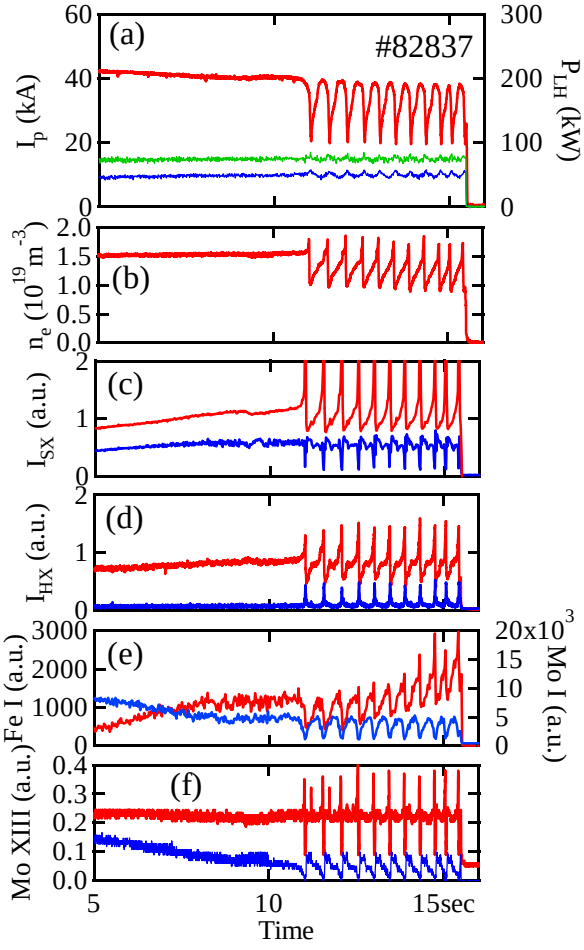

Fig. 14 The typical waveforms of (a)Ip and P_{LH}, (b) n_e, (c)$I_{SX}(0)$(red) and $I_{SX}(7.8cm)$ (blue), (d) $I_{HX}(0)$(red) and $I_{HX}(5cm)$(blue), (e) FeI(red) and MoI (blue), and (f) MoXIII at r=3.7 cm (red) and 7.4cm (blue).

In order to analyze the power hysteresis and the transition between two states whose performance are classified into two categories, the concept of a life time [30,31] for particular performance state to be remained against the external power change has been introduced and the forward transition probability ($1/\tau_{life}$) from the non-ECD mode to the ECD mode has been investigated as a function power in the threshold power window [1,32]. It shows a logarithmic dependence on P_{LH} above the threshold power P_{th} of ~ 80 kW. The backward transition probability was investigated in the power step down experiments. Figure 13 shows a difference from the forward one, that is, τ_{life} is independent of P_{LH} until it decreases very close to P_{th} and the probability ($1/\tau_{life}$) to the non-ECD mode rapidly increases with decreasing P_{LH} around P_{th}. Here the pulse width of LHW was limited for 5 s to avoid the technical heat load problem on the ML. However we confirmed that the ECD mode at P_{LH}=100kW could last for ~20 s. Therefore τ_{life} for the reduced power is expected to be the minimum value. Compared with the logarithmic dependence for the forward transition, it is considered that the appearance of ITB in the intermediate state and sharp boundary of $1/\tau_{life}$ for the back transition causes a power hysteresis, which is characterized by $P_{forward}$ is always higher than $P_{backward}$.

3-4 Sustainment of ECD/ITB and relaxation oscillations

As the ECD is obtained at higher power, it becomes to be difficult to sustain it. It has been observed that the local PWI (hot spot) concerning with the lost energetic electrons leads to terminate the ECD discharge [17]. The Mo armor plates are installed on the four welded parts on the top of the vacuum chamber, where are related with the error fields produced by the fractional turns and ripple trapped energetic electrons. Although Fe, Cr, and Ni influxes are not observed from these parts, additional source is observed from the side part of the ML, where is not enough covered by the Mo

armor. Thus the longest sustained duration of the ECD was limited 26 s in total discharge time of 36 s including a back-transition phase of the non-ECD mode.

As an obstacle to the sustainment of the ECD a relaxation oscillation, self-organized slow sawtooth oscillation (SSSO)[29], appeared, as shown in Fig. 14.The experimental conditions are as follows; P_{LH}~135 kW, B=7 T, $n_e=1.5\times10^{19}m^{-3}$, and two $N_{||}$ values of 1.8 (fixed) and 1.8-2.8(variable) of LHW. Here, $N_{||}$ is the parallel index of refraction. In this experiment a scenario of $j_{LH}(r)$ control by combined $N_{||}$ spectrum LHWs is conducted to sustain the ECD/ITB [33]. As shown in Fig. 14, oscillations with the period of up to 0.5 s are observed on several signals. In this discharge two LHWs with $N_{||}$ of 1.8 and 2.0 are combined from 4 s. The Ip decreased gradually and I_{SX}, I_{HX}, and FeI were increased, while the density remained constant. It is considered that η_{CD} is affected by impurity build-up. At t=11 sec, an oscillation appears and then it continues until the end of the discharge. The plasma is terminated by rf turn-off and not by SSSO itself. As Ip is decreased, n_e, I_{SX}, and I_{HX} are increased significantly, and then they drop below reference levels before SSSO. They increase gradually and reach the reference levels. After that this cycle is repeated. During this cycle FeI and MoI from the ML show the similar oscillations, but there is a different point between them and their oscillations are different from Ip, n_e, I_{SX}, I_{HX} and Mo XIII. At first both decay similarly, but phase difference proceeds with time. During the gradual rise phase MoI starts to decay while FeI continues to increase. This phase difference becomes significant toward the end. The level of FeI increases and the sharp spike appears before they start to decay. The level of MoI is unchanged. It is considered that the position of hot spot moves toward the uncovered area in time or the lost electrons changes in time. The repetition time of SSSO cycle becomes short.

3-5 Change in ITB structure during SSSO

The details of the ITB structure are shown in the expanded time scale. Figure 15 shows the sequence near the crash of the SSSO. Although Ip decays gradually for 0.12 s from t=8.63 s, variations of others are relatively small. At t=8.75 s, n_e and I_{SX}^{peak} starts to grow and then n_e stops to grow at t~8.78 s, while I_{SX}^{peak} continues to increase. As the width of ISX becomes from 60 mm to 20 mm for 0.05 s, that is, an extremely peaked profile is formed. These observations indicate that the ITB foot moves toward the center and the gradient near the foot continues to be steep just before the crash at t=8.8 s. This process is followed by the analyzing the ratio of I_{HX}/I_{SX}, which is assumed to be a measure of $j_{LH}(r)$. Three ratios at $\langle r\rangle_{tan}$=0 cm, 2.5 cm (inside ITB), and 5 cm (ITB foot) are shown. At t=8.75 s $I_{HX}/I_{SX}(0)$ decreases first, then I_{HX}/I_{SX}(5 cm) lag to increase. According to our assumption of $I_{HX}/I_{SX} \propto j_{LH}(r)$, this change suggests that the current profile becomes hollow and at the same time the peak position of $j_{LH}(r)$ moves toward the center, that is, the ITB region shrinks. Finally the steepest gradient causes a radial crash, and then n_e drops abruptly and the impurity is exhausted from the core. The impurity transport analysis and identification of the instabilities are left for future.

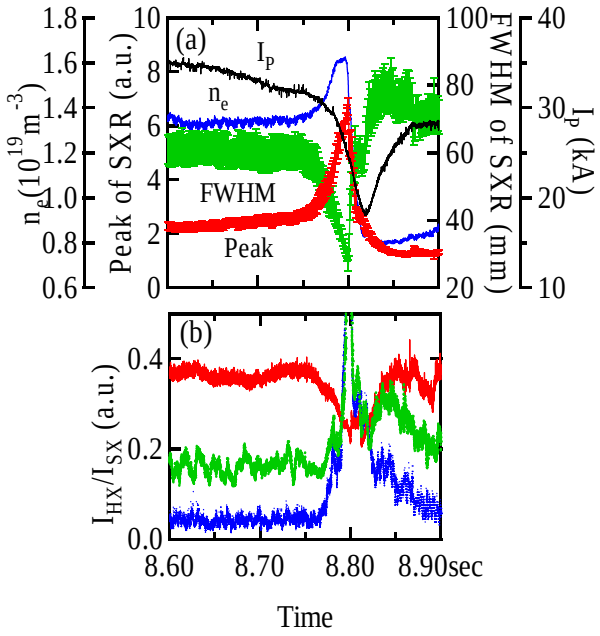

Fig. 15 (a) I_P, n_e, I_{SX} (0) and FWHM of I_{SX} profile, and (b) the ratio of I_{HX} to I_{SX} at r=0 cm (red), 2.5(green), and 5 cm(blue).

4 ECCD of OX-mode at the fundamental electron cyclotron frequency

4-1 ITER relevant steering antenna and relativistic Doppler resonance

The ECH/ECCD experiments at 170 GHz using the TER relevant remote steering antenna were carried out for the first time in the world [34]. The antenna is installed perpendicularly to the magnetic filed in the mid-plane and the steering angle θ_{launch} can be chosen in ±8°-19° corresponding to $N_{||}^{max}$ of ±0.33, in addition to the angle near 0° [35]. The maximum power that transmits through the antenna is 200kW with an efficiency of 95%. Two grooved mirror polarizers are located in the transmission line to optimize the elliptical polarization for the oblique injection.

The electron cyclotron resonance $f=f_{ce}(r)$ is not accessible for the X-mode wave launched from the low field side, because of the right hand cutoff. OX-mode wave can propagate near the cutoff region, bend parallel to the toroidal magnetic filed, and finally interact strongly with the electrons because they have the wave electric vector rotating in the same direction as the electron gyration. The fundamental resonance condition is $\gamma(1-N_{||}v_{||}/c) = f_{ce}/f$, where γ is the relativistic factor, and c and $v_{||}$ the light velocity and electron velocity parallel to the magnetic field line**,** respectively. According to this CD scenario, electrons with several tens of keV in the LHCD plasma can be expected to be resonant with the OX-mode waves, even if the cutoff layer exists. In ref. [14] it has been calculated that the current drive efficiency of OX-mode is higher than that for the O-mode in ITER.

4-2 ECCD by the fundamental X-mode

The experimental conditions are as follows; B=6.25 T-6.55 T (f_{ce}/f = 0.98 -1.04), n_e=0.8-1.2 × 10^{19} m^{-3}, and ECW and LHW power are 100 kW and 60 kW, respectively. For parameters of the target full current drive plasma Ip is 30 kA, η_{CD} ~ 0.3x 10^{19} A/Wm^2 and T_e ~ 400 eV. The pulse width of ECW ranges from 0.2 to 0.5 s and the driven current reaches to a steady state. Figure 16 shows the ΔIp(t) and ΔHX(t) (hard X-ray) at various $N_{||}$ from 0.08 to 0.33. The ΔHX(t) at the major radius is shown. The current grows with a time constant of ~0.03 s as $N_{||}$

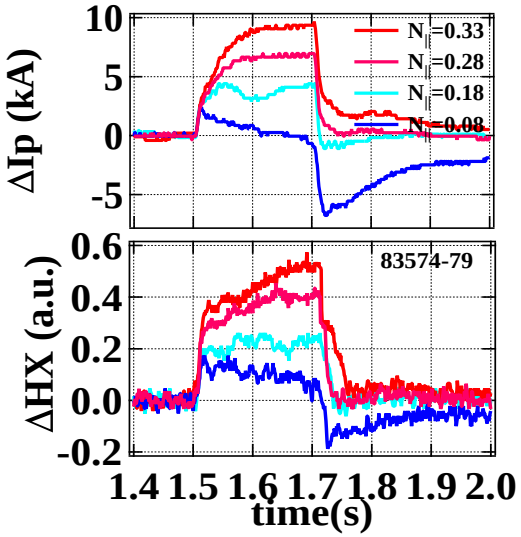

Fig. 16 ΔIp(t) and ΔHX(t) for various $N_{||}$. f_{ce}/f~1 and n_e~1× $10^{19}/m^3$

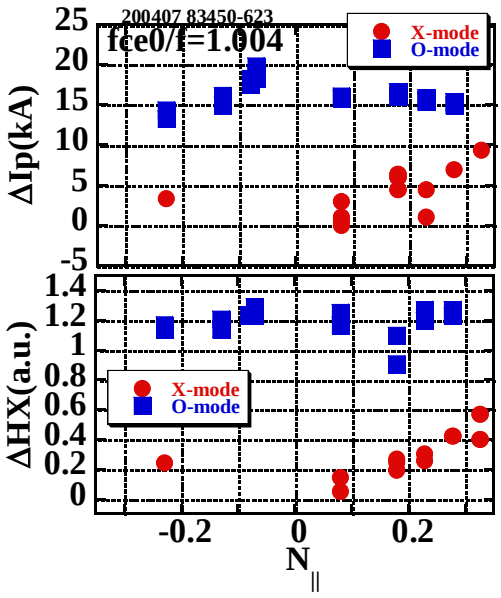

Fig. 17 The $N_{||}$ dependence of ΔIp and ΔHX. For comparison the results for O-mode are also shown.

increases except initial 25 ms, and then saturates at ~ 0.1 s. At $N_{||}$ of 0.33 ΔIp(t) reaches 10 kA and the current is not driven at lower $N_{||}$. At the turn-on phase the negative loop voltage was induced, but it decayed soon. When the ECW is turn off, ΔIp(t) is reduced very quickly compared with the current rising phase and then decays with a longer time constant. It should be noted that above mentioned feature of ΔIp(t) is well reproduced for ΔHX(t). This means that the X-mode resonance actually occurs for energetic electrons. The $N_{||}$ dependence of ΔIp and ΔHX is summarized in Fig. 17. Both ΔIp and ΔHX increase as $N_{||}$ increases above 0.2. This tendency is consistent with the theoretical results. For the negative $N_{||}$ a few kA current was driven as an offset, which was considered to be a contribution of stray O-mode reflected at the cutoff layer and scattered at the wall. Thus net X-mode ECCD driven current ΔIp^{net} = ΔIp($N_{||}$=0.33) - ΔIp($N_{||}$<0)~6kA and the net X-mode ECCD efficiency is ~0.05x10^{19}A/Wm^2 at f_{ce}/f=1.004. The perfect absorption is assumed.

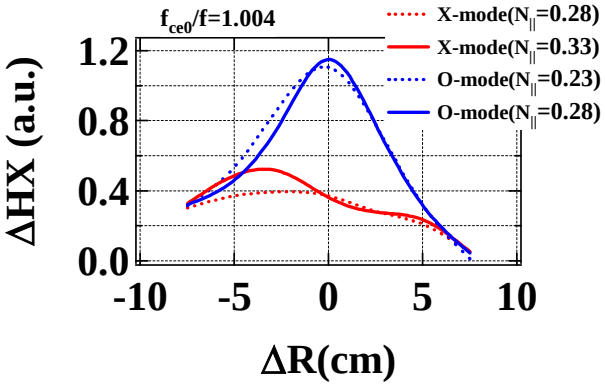

Fig.18 ΔHX profile at $N_{||}$ of 0.33. For comparison O-mode result is also shown.

The off-axis current drive is confirmed by the ΔHX profile, as shown in Fig. 18. The broad profile is observed as $N_{||}$ increases. The in-out asymmetry is not understood. For comparison the O-mode result is also shown, which is characterized by a central peaked profile. This peaked profile is independent of $N_{||}$. The difference between X and O modes is clear. We consider that the driven current in O-mode injection is mainly caused by enhanced LHCD via electron heating and is not a direct evidence of O-mode ECCD. As shown in Fig.17, ΔIp for O-mode ECCD peaked at near the perpendicular injection, and is independent of polarity of $N_{||}$. This fact and no $N_{||}$ dependence of the ΔHX support the hypothesis of enhanced LHCD for O-mode. The combined current drive efficiency $I_p n_e R/(P_{LH}+P_{EC})$ is ~ 0.34 x10^{19}A/Wm^2, which is lower than that for the case of P_{LH}^{total} = $P_{LH}+P_{EC}$. However, for high Te plasma O-mode injection is attractive for on-axis current drive because of applicability at the higher density.

Summary

Experimental results with SSTO, high performance study and current drive are summarized as follows.

The SSTO experiments have been carried out from a view point of control of PWI and wall pumping effects by metal impurity. In the case of the toroidally and poloidally localized PFC, the contribution of the heat load and recycling particles deposited on it are determined. Concerning with the wall pumping in situ measurement of the metal deposition flux and ex situ measurement of the deposition distribution and hydrogen retention are studied and compared with the wall pumping flux determined by the global particle balance. They are consistent with an order of the magnitude. The multi positions measurement will be required. The surface temperature measurement of the heat deposited PFC suggests the existence of significant high temperature dusts in spite of the relatively low bulk temperature. The thermal stability of the dust and effects on the wall pumping should be elucidated. The ULF events characterized by a repetition frequency of 1-2×10^{-3} Hz are found to be as new relaxation oscillations driven by PWI and termination of SSTO is studied.

The understanding of high performance transition physics of the full current drive plasma is progressed. The density and ion ITB can be obtained and the effects of the driven current profile on the ITB formation are clarified. The concept of the life time for the particular performance state to be remained against the external power change is tested for the backward transition, and the transition probability shows a clear difference with respect to the forward transition. Sustainment of the ITB is tackled by controlling the $j_{LH}(r)$ via combination of

LHWs having two different $N_{\parallel}$ spectra. The plasma with ITB can be maintained for 26 sec by the LH power deposited around the foot point of ITB. New relaxation oscillations SSSO concerned with formation and collapse of ITB are found in high performance plasmas. The action of particle exhaust caused by SSSO is preferable to avoid the impurity accumulation.

The scenario of ECCD at the fundamental OX-mode from the LFS is verified at 170GHz in the full current drive plasma at B~ 6T, in which the up-shifted relativistic Doppler resonance condition can be satisfied for the energetic electrons. Applicability and performance of the steering antenna is proved to be available in ITER. The $N_{\parallel}$ dependence of the driven current is consistent with the theoretical predictions and the off-axis current profile is deduced from the hollow HX profile.

Acknowledgements

This work has been partially performed under the framework of joint-use research in RIAM Kyushu University and the bi-directional collaboration organized by NIFS. This work is partially supported by a Grant-in-Aid for Scientific Research from Ministry of Education, Science and Culture of Japan.

References

[1] Zushi H.et al., Nucl. Fusion **43** (2003) 1600.
[2] Jacquinot J et al.,, Nucl. Fusion **43** (2003) 1583.
[3] Houtte van D., et al., Nucl. Fusion **44** (2004) L11.
[4] Zushi H., T. Kuramoto T., et al., 31st EPS (2004) P2.129.
[5] Hirooka Y.,et al., J. N.M. **313-316** (2003) 588.
[6] Zushi H., et al., Nucl. Fusion**41** (2001) 1483-1493.
[7] Hanada K., et al., Nucl. Fusion, **41** (2001) 1539.
[8] Koide Y, Kikuchi M, Mori M, et al., PRL **72** (1994) 3662-3665
[9] Ida K, Shimozuma T, Funaba H, et al., Phys. Rev. Lett. **91** (2003) 085003.
[10] Conner J.W., et al., Nucl. Fusion **44** (2004) R1.
[11] ITER Physics expert Nucl. Fusion **39** (1999) 2495.
[12] Maekawa T., et al., Phys. Rev. Lett. **70** (1993) 2561.
[13] Maehara T., et al., Nucl. Fusion **38** (1998) 39.
[14] Beckmann M. and Leuterer F., Fusion Eng. and Design **53** (2001) 59.
[15] Sakamoto M., et al., Nucl. Fusion **44** (2004) 693.
[16] Shikama,T., Kado S., et al., Physics of Plasma **11** (2004) 4701.
[17] Kuramoto T, Zushi H., et al.,30th EPS **27A** (2003) P2 125.
[18] Sugata T., Hanada K., 12th International Congress on Plasma Physics (2004)P3-094.
[19] Reicle R., et al., J. N.M. **290-293** (2001) 701.
[20] Miyamoto M., et al., 16th PSI (2004) O-69.
[21] Hirai T.,et al., J. Nucl. Mater., **290-293** (2001) 94-98.
[22] Marmar E. S., et al., J. Nucl. Mater., **76-77**(1978) 59.
[23] Nakashima Y., Higashizono Y, private communication (2004).
[24] Fedrici G., et al., Nucl. Fusion **41** (2001) 1967.
[25] Sakamoto M., et al., Nucl. Fusion, **42** (2002) 165-168.
[26] Sakamoto M., et al., this conference Vilamoura (2004) EX/P5-30.
[27] Hirai T.,et al., J. Nucl. Mater., **283-287** (2000) 1177-1181.
[28] Zushi H., et al., 12th International Congress on Plasma Physics Nice (2004)P1-082.
[29] Hanada K., et al., this conference Vilamoura (2004) EX/P4-25.
[30] Itoh S.I., Itoh K., Journal of the Phys. Soc. of Japan, **69** (2000) 427.
[31] Itoh S.I., Itoh K. and Toda S., Phys. Rev. Lett. **89** (2002) 215001.
[32] Ryter F., H-mode database working group, Nucl. Fusion, **36** (1996) 1217.
[33] Hanada K., et al., Journal of Plasma and Fusion Research **77** (2001) 294-299.
[34] Idei H, et al., Proceedings of 13th Joint Workshop on ECE and ECRH, 2004.
[35] Ohkubo K., et al., Fusion Eng. and Design **65** (2003) 657.